



Seismostratigraphy and Thermal Structure of Earth's Core-Mantle Boundary Region

R. D. van der Hilst, *et al.*
Science **315**, 1813 (2007);
DOI: 10.1126/science.1137867

The following resources related to this article are available online at www.sciencemag.org (this information is current as of April 4, 2007):

Updated information and services, including high-resolution figures, can be found in the online version of this article at:

<http://www.sciencemag.org/cgi/content/full/315/5820/1813>

Supporting Online Material can be found at:

<http://www.sciencemag.org/cgi/content/full/315/5820/1813/DC1>

A list of selected additional articles on the Science Web sites **related to this article** can be found at:

<http://www.sciencemag.org/cgi/content/full/315/5820/1813#related-content>

This article **cites 18 articles**, 5 of which can be accessed for free:

<http://www.sciencemag.org/cgi/content/full/315/5820/1813#otherarticles>

This article appears in the following **subject collections**:

Geochemistry, Geophysics

http://www.sciencemag.org/cgi/collection/geochem_phys

Information about obtaining **reprints** of this article or about obtaining **permission to reproduce this article** in whole or in part can be found at:

<http://www.sciencemag.org/about/permissions.dtl>

Seismostratigraphy and Thermal Structure of Earth's Core-Mantle Boundary Region

R. D. van der Hilst,^{1*} M. V. de Hoop,² P. Wang,¹ S.-H. Shim,¹ P. Ma,³ L. Tenorio⁴

We used three-dimensional inverse scattering of core-reflected shear waves for large-scale, high-resolution exploration of Earth's deep interior (D'') and detected multiple, piecewise continuous interfaces in the lowermost layer (D'') beneath Central and North America. With thermodynamic properties of phase transitions in mantle silicates, we interpret the images and estimate in situ temperatures. A widespread wave-speed increase at 150 to 300 kilometers above the core-mantle boundary is consistent with a transition from perovskite to postperovskite. Internal D'' stratification may be due to multiple phase-boundary crossings, and a deep wave-speed reduction may mark the base of a postperovskite lens about 2300 kilometers wide and 250 kilometers thick. The core-mantle boundary temperature is estimated at 3950 ± 200 kelvin. Beneath Central America, a site of deep subduction, the D'' is relatively cold ($\Delta T = 700 \pm 100$ kelvin). Accounting for a factor-of-two uncertainty in thermal conductivity, core heat flux is 80 to 160 milliwatts per square meter (mW m^{-2}) into the coldest D'' region and 35 to 70 mW m^{-2} away from it. Combined with estimates from the central Pacific, this suggests a global average of 50 to 100 mW m^{-2} and a total heat loss of 7.5 to 15 terawatts.

At a depth of ~ 2890 km, the core-mantle boundary (CMB) separates turbulent flow of liquid metals in the outer core from slowly convecting, highly viscous mantle silicates. The 200- to 300-km-thick thermochemical boundary layer on the mantle side—the so-called D'' layer—is enigmatic (1, 2), but a recently discovered phase transition from perovskite (pv) to postperovskite (ppv) in $(\text{Mg,Fe})\text{SiO}_3$ (3–5) begins to explain seismologically observed complexity [e.g., (6)]. If the ppv transition occurs,

one can, in principle, estimate in situ variations in temperature from the pressure-temperature dependence (that is, the Clapeyron slope) and the seismologically inferred location of the associated interface (7). Steep (conductive) thermal gradients in D'' can produce multiple crossings of the phase boundary, and identification of associated seismic signals offers new opportunities for constraining (local) core heat flux (8, 9).

Seismic (transmission) tomography delineates smooth changes in wave speed associated

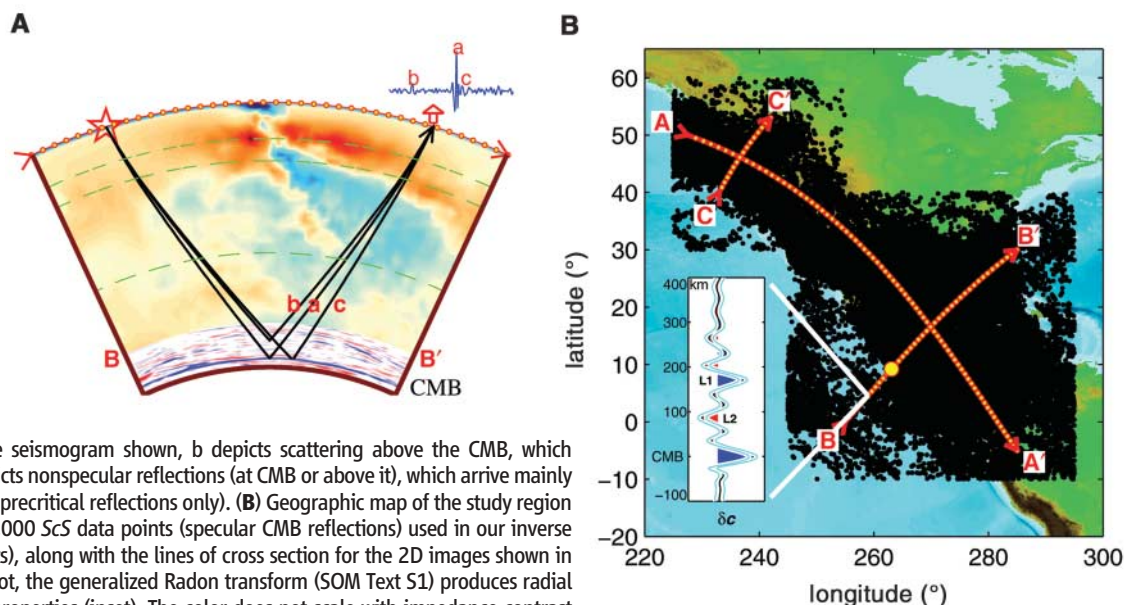
with mantle convection (Fig. 1A), but one must focus on the scattered wave field to image interfaces associated with transitions in mineralogy or composition. Scattering of PKP (the main P wave propagating through the core) in D'' , first recognized in the early 1970s (10), has been used to constrain stochastic models of deep mantle structure [e.g., (11)], but the most detailed and accurate constraints on D'' structure to date have come from forward modeling of shear waves reflected at or near the CMB (12, 13). This approach has its drawbacks, however. First, it requires prior knowledge about the target structure and often assumes relatively simple geometries, the uniqueness of which is not easily established. Second, it relies on signal associated with near- and postcritical incidence, which limits radial resolution and the CMB regions that can be studied (14). The small distance window can also reduce the available source-receiver azimuths, which can degrade imaging in directions perpendicular to dominant sampling (15).

Stacking of data from dense source and receiver arrays can enhance weak signals and has begun to produce tantalizing images of D'' stratification (9, 15, 16). However, most applications still rely on near-critical data and require strict data selection and visual inspection

¹Department of Earth, Atmospheric, and Planetary Sciences, Massachusetts Institute of Technology, Cambridge MA, USA. ²Center for Computational and Applied Mathematics, Purdue University, West Lafayette, IN, USA. ³Department of Statistics, University of Illinois, Urbana-Champaign, IL, USA. ⁴Mathematical and Computer Sciences, Colorado School of Mines, Golden, CO, USA.

*To whom correspondence should be addressed. E-mail: hilst@mit.edu

Fig. 1. (A) In the mantle, tomography depicts smooth P -wave speed variations (45) associated with deep subduction (blue structure in center of section) beneath Central America; inverse scattering constrains deep mantle reflections in the lowermost 400 km. Superimposed on the tomography/scattering image are schematic ray paths of ScS waves reflecting at and above the CMB: a depicts specular CMB reflections, which contribute to the main ScS arrival in the seismogram shown, b depicts scattering above the CMB, which produces precursors, and c depicts nonspecular reflections (at CMB or above it), which arrive mainly in the coda of ScS (we consider precritical reflections only). **(B)** Geographic map of the study region with bounce points of the $\sim 80,000$ ScS data points (specular CMB reflections) used in our inverse scattering study (17) (black dots), along with the lines of cross section for the 2D images shown in Figs. 2 and 3. At each yellow dot, the generalized Radon transform (SOM Text S1) produces radial profiles of contrasts in elastic properties (inset). The color does not scale with impedance contrast but with the reflection coefficient (14) (blue, $R > 0$; red, $R < 0$). Only structure outside the 75% confidence level (thin lines) is discussed here.



tion, which prohibits application to very large data sets

Large-Scale Deep Earth Exploration Seismology

Systematic three-dimensional (3D) imaging of large D'' regions becomes feasible if one can (i) rely on fewer a priori assumptions, so that structures of unknown geometries can be detected; (ii) use efficient methods to detect, extract, and interpret subtle signals in large volumes of broad-band waveforms available through modern data centers; (iii) use data from more source-receiver distances; and (iv) validate results by means other than labor-intensive forward modeling. To achieve this, we combine inverse scattering—specifically, a generalized Radon transform (GRT) of the wave field comprising core-reflected shear waves (ScS) (SOM Text S1)—with statistical methods (SOM Text S2) to produce images of D'' structure and to estimate their uncertainty. This approach benefits from the superior 3D sampling afforded by narrow- and wide-angle data (SOM Text S3) and requires few a priori assumptions about target structures and no visual inspection of data.

For the source-receiver distances considered, specular (mirror-like) reflections of interfaces above the CMB arrive before ScS proper, whereas nonspecular CMB reflections arrive after the main phase (Fig. 1A). The GRT uses data redundancy to identify coherent signal from (single) scattering and localizes the causative structures (17). Statistical inference, a nonlinear process that replaces stacking, suppresses the effects of uneven source-receiver distribution, incorrect wave-speed models, and multiple scattering, and yields rigorous Bayesian confidence levels (18). The latter is used as the initial tool for model validation, which allows routine analysis.

We used ~80,000 broad-band (1 to 20 s) records of the ScS wave field for large-scale, high-resolution exploration of the D'' beneath Central and North America (Fig. 1B) (SOM Text S3). The GRT maps data from wide angles [epicentral distances between 43° and 80° (fig. S3)] into multiple images of the same structure (as illustrated in fig. S1), which are then combined into a radial profile of medium contrasts at a specified CMB location (Fig. 1B, inset). These reflectivity profiles are aligned on the CMB and corrected for 3D mantle heterogeneity inferred from global tomography (19). Juxtaposition of these radial profiles produces 2D (or 3D) images that reveal the lateral extent of medium contrasts and lowermost mantle stratification (fig. S2). Figure 2 clearly reveals the CMB beneath the Americas, but our subject is the rich pattern of scatterers and interfaces up to 400 km above it.

D'' Structure and Temperature

Figure 3 displays the GRT images (top) along with variations in S -wave speed, $d\ln V_s$, derived

from tomography (bottom). To emphasize the relations among them, we superimpose the strongest scatterers (at more than 75% confidence) on the wave-speed maps. We focus on the structures labeled L1, L2, and L3.

Postperovskite transition. Structure L1 delineates an increase of wave speed with depth. In most places L1 is unambiguous because the amplitude of the pulses that define it can be a

substantial fraction of the CMB peak (Fig. 1B, inset), depending on the angle at which L1 is sampled (fig. S1). Our GRT results pertaining to L1 corroborate more localized previous studies of the main D'' discontinuity beneath Central America [see table 1 in (15)], but they also constrain structure far into previously uncharted D'' territory. The depth variation of L1 correlates strongly with changes in S -wave speed (20). If

Fig. 2. Three-dimensional exploration seismology of the lowermost mantle. Seismic images of the lowermost mantle (CMB to 400 km above it) are produced by lateral juxtaposition of radial general Radon transform profiles (fig. S2) calculated at image points along the section lines shown in Fig. 1. Structure outside 75% confidence bands (18) includes the CMB (at 0 km) and several scatter interfaces above it. Thinly dashed lines indicate scatter interfaces (L1, L2) highlighted in Fig. 3. This 3D rendition illustrates the large spatial scales over which inverse scattering with the ScS wave field can be used to explore the lowermost mantle. Points X1 and X2 indicate the section intersections. The background color depicts the prediction of the height above the CMB of a presumed phase transformation with a Clapeyron slope of 6 MPa/K (21). In most of this region, the correlation between L1 and the predicted values is very good

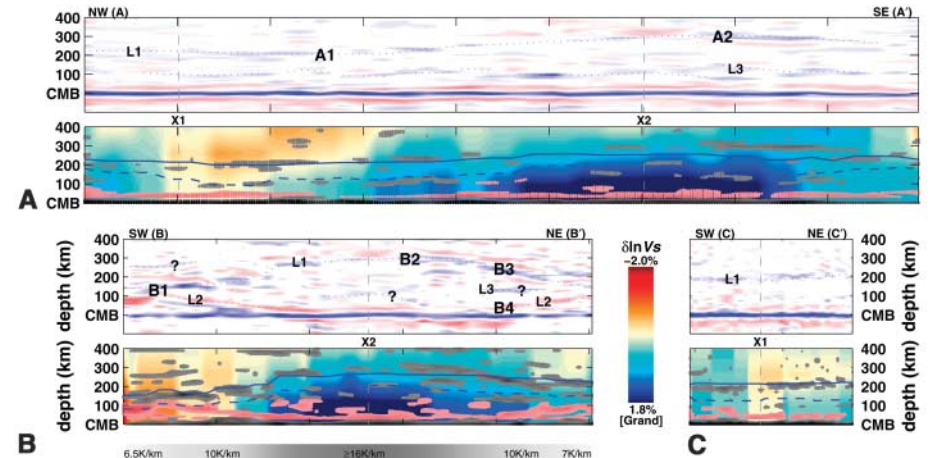
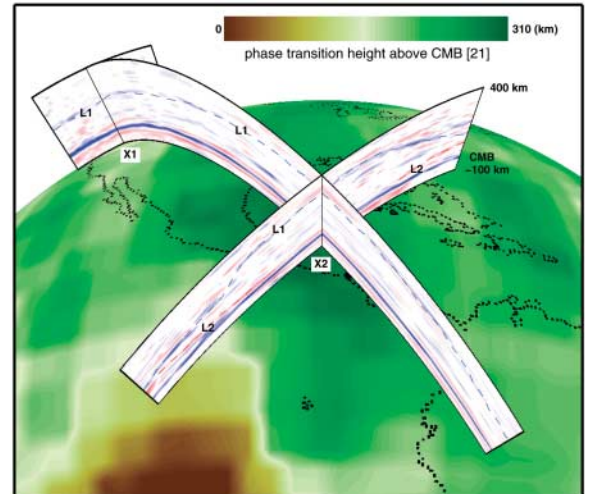


Fig. 3. Reflectivity from inverse scattering, at more than 75% confidence (18) (top) and S -speed ($d\ln V_s$) from tomography (19) (bottom). Scatter images are obtained by interpolation between GRT profiles (Fig. 1B, inset) calculated every 1° (~60 km at CMB) along sections A-A', B-B', and C-C' in Fig. 1. For the frequencies and incidence angles used, the radial resolution is ~10 km. The color scale for tomography is given between B-B' and C-C'. (A) L1, L2, and L3 label the scatter interfaces (thinly dashed). (B and C) The associated scatterers (visually enhanced) are superimposed on the tomography profiles, with dark gray depicting positive reflections and pink/red negative contrasts. Interface L1 aligns increases of wave speed with increasing depth; L2 delineates a decrease; L3 is more ambiguous but generally coincides with a wave-speed increase. Whereas L1 and L2 are piecewise continuous, L3 has an intermittent, en echelon appearance. The solid (dashed) blue lines in the bottom panels depict the phase transition location predicted by (21) (22). Points A1 and A2 and points B1 to B4 on L1 and L2 are used for temperature calculations (Fig. 4). The gray scale below B-B' depicts the lateral variation in temperature gradient along the CMB (for $\gamma_{ppv} = 10$ MPa/K) estimated from (29). In the central portion of the section, dT/dz cannot be determined directly because the occurrence of the double crossing cannot be resolved.

the latter is (partly) of thermal origin, the GRT images provide direct evidence for a widespread presence of a D'' interface with a positive pressure-temperature relationship.

Sidorin *et al.* (21) postulated that a phase transition with Clapeyron slope $\gamma = 6 \text{ MPaK}^{-1}$ marks the top of D''. A recent analysis (22) puts the main discontinuity $\sim 95 \text{ km}$ deeper (dashed blue line, Fig. 3), but the original prediction (solid blue lines) is quite close to L1. The larger topography on the latter suggests that γ is more than 6 MPaK^{-1} , which is consistent with estimates from mineral physics for the ppv transition (7), or that the actual wave-speed variations are larger than inferred tomographically. If, indeed, interface L1 marks the ppv transition, we can estimate in situ mantle temperatures from its topography (Fig. 4). For $\gamma_{\text{ppv}} = 10 \text{ MPaK}^{-1}$, the temperatures at B1 and B2 are ~ 2000 and $\sim 2900 \text{ K}$, respectively, and the difference between A1 and A2 is $\sim 600 \text{ K}$.

On long wavelengths (1000 to 2000 km), the changes in temperature along L1 reflect the shoaling of the phase boundary toward D'' regions where relatively cool slab debris can be expected. Changes on a scale of $\sim 450 \text{ km}$ relate

to the margins of these regions and to localized slow regions. Steeper topography is observed locally, for instance at $\sim 800 \text{ km}$ along section B-B', which is close to a steplike jump previously attributed to folding of subducted slab (23). Seismic tomography (Fig. 1A) and the above temperature differences both support the presence of slab debris, and slab buckling is indeed likely to occur in this region (24). Drawing conclusions from isolated structures can be misleading, however, and partial reconstruction of multiple scatter interfaces can produce ambiguity. Interface L1 aligns the strongest scatterers and is consistent with (21), but we cannot rule out that between 0 and 800 km (in section B-B') it continues southeastward with little topography and that the stronger structure at $\sim 150 \text{ km}$ represents interface L3.

Postperovskite lens? The GRT images reveal much structural complexity between the CMB and L1, the presumed top of D''. Particularly intriguing is a wave-speed reduction (producing the negative pulse, L2, in Fig. 1B, lower left) that delineates a large-scale ($\sim 2300 \text{ km}$) concave-up interface in the lowermost 100 km or so of the mantle. Because of side lobes of the CMB

reflection, L2 cannot be established between 1000 and 2000 km along B-B', but interfaces that dip toward the seismologically fast central region are resolved on either side of this patch. In this region, (15) reported a wave-speed decrease further above CMB and more parallel to the top D'' interface.

Published estimates of CMB temperature T_{cmb} vary from 3750 K to 4800 K (25–27), and most exceed T_{ppv} . The latter implies that ppv is unstable near the CMB and that there is a second crossing of the phase boundary. The back transition (ppv \rightarrow pv) occurs deeper in colder regions (Fig. 4), thus creating ppv lenses beneath mantle downwellings (8, 16). This transition is hard to detect (28), but recent studies provide evidence for it in the lowermost mantle beneath the Pacific (9) and the Cocos plate (22). In our GRT profiles, the negative pulses are statistically significant (Fig. 1 and fig. S2), and both the sign and the deepening toward regions of presumably lower D'' temperatures is consistent with ppv \rightarrow pv. The presence of L2 and the anticorrelated topographies of L1 and L2 provide new evidence that ppv-rich lenses do indeed exist. The lens beneath Central America has a width of $\sim 2300 \text{ km}$ and a thickness of $\sim 250 \text{ km}$; L1 and L2 merge (near B1) $\sim 125 \text{ km}$ above the CMB ($T = 2900 \text{ K}$; $P = 128 \text{ GPa}$). Outside this lens, the temperature may be too high for ppv to be stable, except, perhaps, in regions of iron enrichment (9).

Mantle temperature near CMB. Whereas the ppv transition constrains temperatures some 150 to 300 km above the CMB, double crossings provide insight into the thermal structure closer to the core (8, 9). We know neither T_{cmb} nor the thickness H and temperature change ΔT_{TBL} across a thermal boundary layer (TBL), but with reasonable assumptions we can estimate T_{cmb} and ΔT_{TBL} by fitting error functions to temperatures at L1 and L2 as a function of H (29). H increases from colder to warmer D'' regions. If the CMB is isothermal, and not arbitrarily hot, we obtain stable estimates of T_{cmb} and ΔT_{TBL} for H such that the ppv transition (e.g., at B3) occurs above or near the top of the TBL and the back transition (e.g., at B4) occurs well within it. For $H = 100$ to 200 km and $\gamma_{\text{ppv}} = 10 \text{ MPa/K}$, we infer $T_{\text{cmb}} = 3950 \pm 200 \text{ K}$ and $\Delta T_{\text{TBL}} = 1600$ to 1400 K (Fig. 4C). These values depend on the Clapeyron slope and, in particular, on the phase-boundary temperature at the CMB; we estimate that $T_{\text{cmb}} \approx T_{\text{ppv,cmb}} + 290 \text{ K}$. Our T_{cmb} is lower than, but within error consistent with, the estimate of 4100 K in (9).

Despite large uncertainties, T_{cmb} constrains the melting curve of iron in the liquid core because the temperature just below the CMB must exceed the melting temperature of core materials. Experimental and computational estimates of the melting point of pure Fe at CMB pressures span a range from $3200 \pm 200 \text{ K}$ (30) to $4800 \pm 200 \text{ K}$ (31). Minor elements can reduce this by as much as 700 to 1000 K (27), but

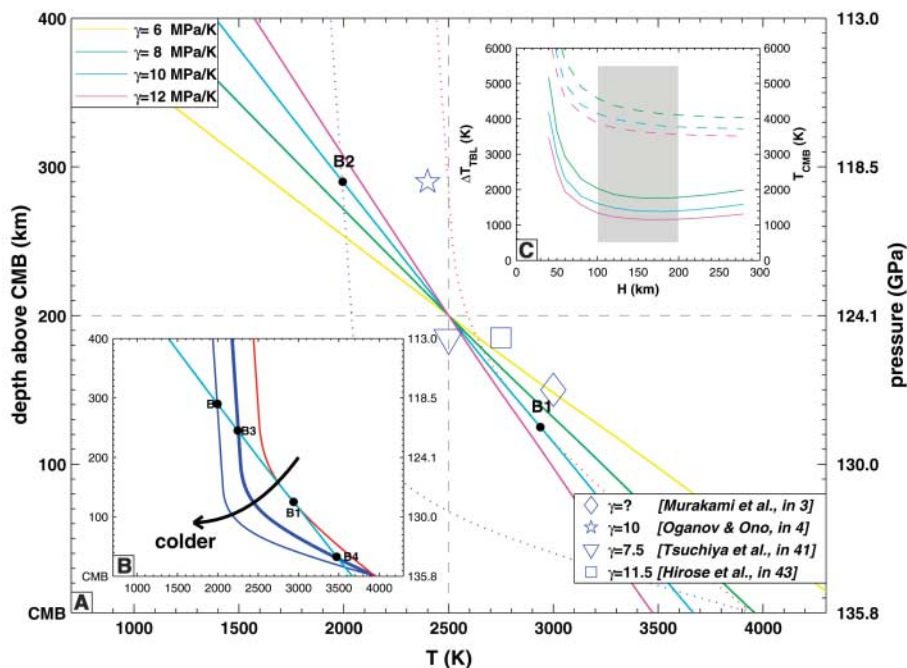


Fig. 4. (A) Temperature (x axis) versus distance above CMB (y axis). As a point of reference for producing absolute temperature and depth (pressure), we assume $P_{\text{ppv}} = 124 \text{ GPa}$ and $T_{\text{ppv}} = 2500 \text{ K}$, and we consider Clapeyron slopes $\gamma_{\text{ppv}} = 6, 8, 10,$ and 12 MPa/K . If L1 in Fig. 3 represents the ppv transition, the temperature at points B1 and B2 can be estimated as $\gamma_{\text{ppv}} = 10 \text{ MPa/K}$, $T_{\text{ppv,B2}} = 2000 \text{ K}$, and $T_{\text{ppv,B1}} = 2900 \text{ K}$. Dotted lines depict estimated geotherms through B1 and B2; the shallow part is adiabatic, but toward the CMB the conductive geotherm is described as an error function (the change of adiabat to conductive is not known, however). (B) Cold, intermediate, and hot geotherms. As the mantle temperature decreases, a ppv transition occurs at increasing distances above CMB, and a second crossing would occur at decreasing height above CMB. The geotherm through the ppv transition (B3) and the back-transition (B4) is calculated (29) using a thickness of the hypothetical boundary layer, H , of 150 km . (C) Mantle temperature, T_{cmb} , at the CMB (dashed lines) and the temperature change, ΔT_{TBL} , across the thermal boundary layer (solid lines) as a function of TBL thickness, H , and for $\gamma_{\text{ppv}} = 8, 10,$ and 12 MPa/K . Stable estimates are obtained for $H = 100$ to 200 km (gray shading).

experiments reveal that for oxygen and sulfur the effect is small (32). If $T_{\text{cmb}} = 3950 \pm 200$ K, the melting point in (31) may thus be too high.

Core heat flux. To estimate heat flux, we need to know thermal conductivity κ and the temperature gradient dT/dz across the TBL. A lower bound on the latter is given by γ_{ppv}^{-1} (8); for $\gamma_{\text{ppv}} = 7$ to 10 MPa/K, this implies $dT/dz|_{\text{min}} = 5.8$ to 8.3 K/km. The gradient must be steeper than γ_{ppv}^{-1} for a double crossing to occur. Our temperature estimates imply gradients of 7 to 16 K/km (Fig. 3B).

Even if we assume that these gradients are reasonably accurate, the regional and, in particular, global heat flux remains subject to considerable uncertainty. First, the region where dT/dz can be estimated does not span a diverse geodynamical environment. We consider the steep gradients as representative of cold D'' areas. Our study region does not include large-scale low wave-speed regions, where higher mantle temperatures and lower gradients are expected. We could speculate that our regional minimum (~ 7 K/km) is close to the global average, but this would be a lower bound if the anomalously low wave speeds are (in part) due to chemistry [e.g., (33)]. Lay *et al.* (9) consider effects of iron and estimate the thermal gradient beneath the central Pacific at 8.5 ± 2.5 K/km.

Second, the value of thermal conductivity is debated. The often-used $\kappa = 10 \text{ Wm}^{-1}\text{K}^{-1}$ (25) would imply a regional variation in heat flux q_{cmb} of $115 \pm 45 \text{ mWm}^{-2}$, compared with $85 \pm 25 \text{ mWm}^{-2}$ below the Pacific (9). If one assumes that these regional values represent extremes, a reasonable average flux would be $q_{\text{cmb}} \approx 100 \text{ mWm}^{-2}$ (corresponding to a global heat loss across the CMB of ~ 15 TW). However, κ may be as small as $5 \text{ Wm}^{-1}\text{K}^{-1}$ (34, 35). Depending on the amount of radiative conduction, the conductive component to the heat loss across the CMB is thus uncertain by (at least) a factor of two ($Q_{\text{cmb}} \approx 7.5$ to 15 TW). It is likely, however, that the flux into the base of the mantle exceeds the heat conducted down the core adiabat, which has implications for models of thermal core-mantle coupling, core evolution, and the distribution of heat-producing elements (36, 37).

Other D'' interfaces? Over the entire geographical region studied here, the GRT images suggest the presence of scatterers (L3 in Fig. 3) some 100 km below the presumed top of the D''. Further study is required to establish whether it is the partial detection of a continuous interface (or multiple interfaces) or whether it represents a depth range with intermittent, en echelon scatter zones. The sign of change in elastic properties is not unequivocal because of ambiguity between main pulse and side lobes. Positive and negative changes may both occur, but variations in S-wave speed in this depth interval suggest the preponderance of radial increases in wave speed.

Slab folding (16, 24), along with preserved compositional heterogeneities, can perhaps pro-

vide the complexity detected here. Alternatively, local changes in temperature or chemical composition [e.g., in iron content (38) or partitioning between pv and magnesiowüstite (39)] can readily create multiple crossings of the phase boundary. Alternating, irregular ppv and pv lenses (or layers) may be more realistic than a single ppv lens (40) and can explain some of the multiple, but intermittent, scatter interfaces. This calls for further investigation by means of joint imaging and geodynamical and petrological modeling.

New Opportunities for Deep-Earth Imaging

The results presented here should be regarded as first steps, but they show the potential of using inverse scattering techniques originally developed to search for hydrocarbon reservoirs for the systematic, high resolution investigation of the lowermost mantle over large regions, including hitherto uncharted D'' territory. Application to Central America allows verification against previous results, but similar high-resolution D'' imaging should be possible elsewhere, for instance, beneath large parts of Eurasia. As we suppose was the case when seismologists pondered over the first reflection profiles of Earth's crust, image quality is not as good everywhere as one would wish, and even first-order observations can be puzzling. However, we expect that refinement of inverse scattering, accounting for increasingly many complexities and using exponentially growing data sets will remove existing ambiguities and provide insight into the structure, dynamics, and evolution of this remote frontier of cross-disciplinary research.

References and Notes

- M. E. Wyession *et al.*, *Geodynam. Ser. (Am. Geophys. Un.)* **28**, 273 (1998).
- E. J. Garnero, *Annu. Rev. Earth Planet. Sci.* **28**, 509 (2000).
- M. Murakami, K. Hirose, K. Kawamura, N. Sata, Y. Ohishi, *Science* **304**, 855 (2004).
- A. R. Oganov, S. Ono, *Nature* **430**, 445 (2004).
- S. H. Shim, T. S. Duffy, R. Jeanloz, G. Shen, *Geophys. Res. Lett.* **31**, L10603 (2004).
- J. Wookey, S. Stackhouse, J.-M. Kendall, J. Brodholt, G. D. Price, *Nature* **438**, 1004 (2005).
- Relevant here are the pressure P (or depth, z) and temperature T of the ppv transition and the Clapeyron slope γ of the phase boundary in P - T space, all of which have considerable uncertainties. Published values include $P_{\text{ppv}} \sim 110$ to 125 GPa, $T_{\text{ppv}} \sim 2200$ to 2700 K, and $\gamma_{\text{ppv}} \sim 7$ to 11.5 MPaK $^{-1}$ (4, 41–43). We convert depth to pressure according to the Preliminary Reference Earth Model (PREM) (44).
- J. W. Hernlund, C. Thomas, P. J. Tackley, *Nature* **434**, 882 (2005).
- T. Lay, J. Hernlund, E. J. Garnero, M. S. Thorne, *Science* **314**, 1272 (2006).
- J. R. Cleary, R. A. W. Haddon, *Nature* **240**, 549 (1972).
- M. A. H. Hedlin, P. M. Shearer, P. S. Earle, *Nature* **387**, 145 (1997).
- T. Lay, E. J. Garnero, *Geophys. Monogr. Ser.* **150**, 25 (2004).
- D. V. Helmberger, T. Lay, S. Ni, M. Gurnis, *Proc. Natl. Acad. Sci. U.S.A.* **102**, 17257 (2005).
- For given impedance contrast, the reflection coefficient R increases with scatter angle, or epicentral distance, in particular toward the critical angle (fig. S1). Wide-angle data can produce strong peaks in the stacks even for weak interfaces, which allows modeling, but radial resolution is diminished because the dependence of travel time on interface position vanishes for near grazing incidence. Near- and postcritical D'' reflections and refractions arrive at $\sim 74^\circ$ to 85° from the source, but modeling studies often use even narrower distance ranges (e.g., 79° to 82°). With nonuniform source and receiver distributions, narrow distance ranges can imply narrow source-receiver azimuths. The latter may, effectively, turn 3D techniques into 2D probes. We use data in a much larger distance range (43° to 80° , with most data between 50° and 70°); see fig. S3. The inclusion of relatively narrow angle data enhances radial resolution (fig. S1) and allows more complete 3D data coverage.
- C. Thomas, E. J. Garnero, T. Lay, *J. Geophys. Res.* **109**, B08307 (2004).
- A. Hutko, T. Lay, E. J. Garnero, J. Revenaugh, *Nature* **441**, 333 (2006).
- P. Wang, M. V. de Hoop, R. D. van der Hilst, P. Ma, L. Tenorio, *J. Geophys. Res.* **111**, 10.1029/2005JB004241 (2006).
- P. Ma, P. Wang, L. Tenorio, M. V. de Hoop, R. D. van der Hilst, *J. Geophys. Res.*, Manuscript available at <http://quake.mit.edu/hilstgroup/robospace/PapersPDF/2006JB004513R.pdf>.
- S. P. Grand, *Philos. Trans. R. Soc. London A* **360**, 2475 (2002).
- Upon image construction, we correct for 3D variations in S-wave speed (19), but the location of the scatterers (discontinuities) could be biased toward (or away from) the CMB in regions where the actual wave speed is higher (or lower) than inferred from tomography. This is the opposite of the observed trend, which suggests that the actual topography (and the Clapeyron slope or temperature variation inferred from it) could be larger than inferred here.
- I. Sidorin, D. V. Helmberger, M. Gurnis, *Science* **286**, 1326 (1999).
- D. Sun, T.-R. A. Song, D. Helmberger, *Geophys. Res. Lett.* **33**, L12507 (2006).
- Hutko and co-workers (16) observe a steplike jump in a north-south section (their A-A'), whereas we see it best in a southwest-northeast section (B-B'). This is no contradiction; both may sample different (but nearby) parts of a 3D, northwest-southeast trending structure.
- N. Ribe, E. Stutzmann, Y. Ren, R. D. van der Hilst, *Earth Planet. Sci. Lett.* **254**, 173 (2007).
- F. Stacey, *Physics of the Earth* (Brookfield, Kenmore, Queensland, Australia, ed. 3, 1992).
- D. Alf e, M. J. Gillan, G. D. Price, *Earth Planet. Sci. Lett.* **195**, 911 (2002).
- E. Knittle, R. Jeanloz, *J. Geophys. Res.* **96**, 16169 (1991).
- C. Flores, T. Lay, *Geophys. Res. Lett.* **32**, 10.1029/2005GL024366 (2005).
- Absent knowledge about the behavior of the conductive geotherm in this complex thermochemical boundary layer, we use $T(z) = T_{\text{cmb}} - \Delta T_{\text{HS}} \text{erf}(z/H)$, with error function (erf) describing heat diffusion into a half space and ΔT_{HS} the total temperature contrast across the half space. From ΔT_{HS} , we estimate the contrast across the TBL as $\Delta T_{\text{TBL}} = \text{erf}(1)\Delta T_{\text{HS}} = 0.84\Delta T_{\text{HS}}$. For different Clapeyron slopes, we calculate $T(B3)$ and $T(B4)$. For a given diffusion length H , we can then find a unique solution of T_{cmb} and ΔT_{TBL} .
- R. Boehler, *Nature* **363**, 534 (1993).
- Q. Williams, R. Jeanloz, J. Bass, B. Svendsen, T. J. Ahrens, *Science* **236**, 181 (1987).
- R. Boehler, A. Chopelas, A. Zerr, *Chem. Geol.* **120**, 199 (1995).
- R. D. van der Hilst, H. K arason, *Science* **283**, 1885 (1999).
- A. M. Hofmeister, *Science* **283**, 1699 (1999).
- A. P. van den Berg, E. S. G. Rainey, D. A. Yuen, *Phys. Earth Planet. Inter.* **149**, 259 (2005).
- J. Bloxham, *Philos. Trans. R. Soc. London A* **358**, 1171 (2000).

37. B. A. Buffett, *Science* **288**, 2007 (2000).
 38. W. Mao et al., *Proc. Natl. Acad. Sci. U.S.A.* **101**, 15867 (2004).
 39. Y. Kobayashi et al., *Geophys. Res. Lett.* **32**, 10.1029/2005GL023257 (2005).
 40. S.-H. Shim, *Am. Geophys. Union Geophys. Monogr.* **160**, 261 (2005).
 41. T. Tsuchiya, J. Tsuchiya, K. Umemoto, R. M. Wentzcovitch, *Earth Planet. Sci. Lett.* **224**, 241 (2004).
 42. T. Iitaka, K. Hirose, K. Kawamura, M. Murakami, *Nature* **430**, 442 (2004).
 43. K. Hirose, R. Sinmyo, N. Sata, Y. Ohishi, *Geophys. Res. Lett.* **33**, L01310 (2006).
 44. A. M. Dziewonski, D. L. Anderson, *Phys. Earth Planet. Inter.* **25**, 297 (1981).
 45. H. Káráson, R. D. van der Hilst, *J. Geophys. Res.* **106**, 6569 (2001).
 46. This research is supported by the Collaboration in Mathematical Geosciences program of the U.S. National Science Foundation. All waveform data were obtained through the Data Management Center of the Incorporated Research Institutions for Seismology. We thank D. Sun

(Caltech) for providing their latest ppv model and B. Hager (MIT) and A. van den Berg (Utrecht University) for discussions.

Supporting Online Material

www.sciencemag.org/cgi/content/full/315/5820/1813/DC1
 SOM Text
 Figs. S1 to S3
 References

21 November 2006; accepted 22 February 2007
 10.1126/science.1137867

Computational Design of Peptides That Target Transmembrane Helices

Hang Yin,^{1*} Joanna S. Slusky,^{1*} Bryan W. Berger,¹ Robin S. Walters,¹
 Gaston Vilaire,² Rustem I. Litvinov,³ James D. Lear,¹ Gregory A. Caputo,¹
 Joel S. Bennett,² William F. DeGrado^{1,4,†}

A variety of methods exist for the design or selection of antibodies and other proteins that recognize the water-soluble regions of proteins; however, companion methods for targeting transmembrane (TM) regions are not available. Here, we describe a method for the computational design of peptides that target TM helices in a sequence-specific manner. To illustrate the method, peptides were designed that specifically recognize the TM helices of two closely related integrins ($\alpha_{IIb}\beta_3$ and $\alpha_v\beta_3$) in micelles, bacterial membranes, and mammalian cells. These data show that sequence-specific recognition of helices in TM proteins can be achieved through optimization of the geometric complementarity of the target-host complex.

Transmembrane (TM) helices play essential roles in biological processes, including signal transduction, ion transmission, and membrane-protein folding. Computational (1–4) and genetic methods (5, 6) are available to engineer antibody-like molecules that target the water-soluble regions of proteins; however, companion methods to target the TM regions are lacking. The design of TM helices that specifically recognize membrane proteins would advance our understanding of sequence-specific recognition in membranes and simultaneously would provide new approaches to modulate protein-protein interactions in membranes. Here we describe a computational approach, designated computed helical anti-membrane protein (CHAMP), to design peptides that specifically recognize the TM helices of natural proteins (7).

Computational design. The design of a CHAMP peptide requires the selection of a backbone geometry for the CHAMP peptide-target complex, followed by computational selection of the CHAMP peptide's amino acid sequence with a side-chain repacking algorithm. To simplify the

selection of the backbone geometry, we used the growing database of membrane-protein structures, rather than relying on idealized helical dimers. The majority of the TM helix-helix pairs in TM proteins of known structure fall into a handful of well-defined structural motifs with recognizable sequence signatures (8). Thus, it is possible to predict a preferred mode of interaction between a target TM helix and other TM helices from the amino acid sequence alone. Once a preferred mode of interaction has been identified, examples of helix pairs from proteins of known structure can be used as backbone conformations for the design of a desired CHAMP peptide. The next steps are (i) to thread the sequence of the targeted TM helix onto one of the two helices of the selected pair and (ii) to select the amino acid sequence of the CHAMP helix with a side-chain repacking algorithm (1–4, 9).

As a stringent test of the CHAMP method, we focused on the recognition of the TM domains of two closely related and extensively studied platelet integrins, $\alpha_{IIb}\beta_3$ and $\alpha_v\beta_3$, as convenient biologically important targets (10–12). Both the α_{IIb} and α_v TM helices contain a small- X_3 -small motif, in which G (13) or other small residues (A and S) are spaced four residues apart (14) (Fig. 1, B and C). This sequence motif is associated with a high propensity to interact in a tightly packed “parallel GAS_{Right} motif” (8) with a right-handed helical crossing angle of $\sim 40^\circ$. Indeed, site-directed mutagenesis (15–17) and modeling studies (15, 17, 18) suggest that the α_{IIb} TM helix binds the β_3 TM helix with this geometry.

Five template backbones were tested in the design of a CHAMP peptide directed against α_{IIb} , and 15 were tested for α_v . The sequences of α_{IIb} and α_v were threaded onto either of the two helices in each template, yielding two different CHAMP peptides per template. A sequence for the opposing CHAMP helix was then selected with a Monte Carlo repacking algorithm that considers different combinations of side chains in low-energy rotamers (1–4, 9) [see Supporting Online Material (SOM)]. The rotameric states of the side chains in the target were allowed to vary, as were both the sequence and rotamers of the CHAMP side chains. A simple energy function that is based on a linearly dampened Lennard-Jones potential and a membrane depth-dependent knowledge-based potential (19) was then used to select the desired residues. This knowledge-based potential assured that residues with high propensities to occupy the interfacial and fatty acyl region of the bilayer were selected at appropriate positions. The membrane-exposed residues of the CHAMP helix were then randomly selected with a 60% probability of assigning L and a 10% probability of assigning A, I, F, or V.

The TM domains of α_v and α_{IIb} are highly homologous (Fig. 1, B and C), and they both have small- X_3 -small motifs. Because a number of other integrin TM helices also contain a small- X_3 -small motif, a specific CHAMP peptide must recognize not only this global feature of its target, but also more fine-grained differences in surface topography. In the computed complexes with the lowest energy, the CHAMP sequences designed against α_v and α_{IIb} both have G- X_3 -G sequences that create a shallow concavity that is important for recognizing the small- X_3 -small sequence on the integrin helices. However, the surrounding sequences differ in response to differences in the sequences of the target (Fig. 1, B and C), thereby providing specificity.

A CHAMP peptide with extensive geometric complementarity to its target (Fig. 1D and fig. S1) was selected based on its energy score, the uniformity of packing of the side chains at the CHAMP-target interface, and the ease of synthesis. [Peptides with multiple strings of β -branched amino acids and sequences with particularly high predictions for amyloid (20) were avoided.] The templates for the CHAMP peptide-target complexes were taken from polytopic proteins with no functional or structural relation to integrins, the CHAMP peptide

¹Department of Biochemistry and Biophysics, School of Medicine, University of Pennsylvania, Philadelphia, PA 19104, USA. ²Hematology-Oncology Division, Department of Medicine, School of Medicine, University of Pennsylvania, Philadelphia, PA 19104, USA. ³Department of Cell and Developmental Biology, School of Medicine, University of Pennsylvania, Philadelphia, PA 19104, USA. ⁴Department of Chemistry, University of Pennsylvania, Philadelphia, PA 19104, USA.

*These authors contributed equally to this work.

†To whom correspondence should be addressed. E-mail: wdegrado@mail.med.upenn.edu